ELSEVIER

Nuclear Instruments and Methods in Physics Research A 490 (2002) 71–89

NUCLEAR INSTRUMENTS & METHODS IN PHYSICS RESEARCH Section A

www.elsevier.com/locate/nima

CELESTE: an atmospheric Cherenkov telescope for high energy gamma astrophysics

E. Paré[a,✠], B. Balauge[b], R. Bazer-Bachi[d], H. Bergeret[f], F. Berny[f], N. Briand[d], P. Bruel[a], M. Cerutti[a], J. Collon[f], A. Cordier[f], P. Cornebise[f], G. Debiais[e], J.-P. Dezalay[d], D. Dumora[b], E. Durand[b], P. Eschstruth[f], P. Espigat[c], B. Fabre[e], P. Fleury[a], J. Gilly[a], J.-C. Gouillaud[b], C. Gregory[a], N. Hérault[e,f], J. Holder[f], M. Hrabovsky[g], S. Incerti[b], A. Jouenne[f], L. Kalt[a], R. LeGallou[b], B. Lott[b], O. Lodygensky[f], P. Manigot[a], H. Manseri[a], H. Manitaz[a], M. Martin[f], R. Morano[a], G. Morineaud[a], F. Münz[c,h], A. Musquère[d], M. de Naurois[a], J. Neveu[f], J.-M. Noppe[f], J.-F. Olive[d], M. Palatka[g], A. Perez[b], J. Québert[b], A. Rebii[b], T. Reposeur[b,*], L. Rob[h], P. Roy[f], J.-L. Sans[b], T. Sako[a], P. Schovanek[g], D.A. Smith[b], P. Snabre[i], G. Villard[f]

[a] *Laboratoire Leprince-Ringuet, Ecole Polytechnique, Route de Saclay, F-91128 Palaiseau Cedex, France*

[b] *Centre d'Etudes Nucléaires de Bordeaux-Gradignan, CNRS/IN2P3-Université Bordeaux 1, Domaine du Haut Vigneau, BP 120, F-33175 Gradignan Cedex, France*

[c] *Laboratoire de Physique Corpusculaire et Cosmologie, Collège de France, 11 place Marcelin Berthelot, F-75231 Paris Cedex 05, France*

[d] *Centre d'Etude Spatiale des Rayonnements, 9 avenue du Colonel Roche, BP 4346, F-31028 Toulouse Cedex4, France*

[e] *Groupe de Physique Fondamentale, Université de Perpignan, 52, Avenue de Villeneuve, F-66860 Perpignan Cedex, France*

[f] *Laboratoire de l'Accélérateur Linéaire, Université de Paris-Sud, Bat. 200, BP 34, F-91898 Orsay Cedex, France*

[g] *Joint Lab. Optics, Academy of Sciences and Palacky University, 17, listopadu 50, 77207 Olomouc, Czech Republic*

[h] *Institute of Particles and Nuclear Physics, Charles University, V Holesovickach 2, 180 00 Prague 8, Czech Republic*

[i] *Institut de science et de génie des Matériaux et Procédés, Odeillo, France*

Received 16 April 2002; accepted 18 April 2002

Abstract

CELESTE is an atmospheric Cherenkov telescope based on the sampling method which makes use of the decommissioned THEMIS solar electrical plant in the French Pyrénées. A large (2000 m^2) mirror surface area from 40 independent heliostats followed by a secondary optic, a trigger system using analog summing techniques and signal digitization with 1 GHz flash ADCs make possible the detection of cosmic γ-rays down to 30 GeV. This paper provides a detailed technical description of the CELESTE installation. © 2002 Elsevier Science B.V. All rights reserved.

Keywords: Gamma-ray astronomy; Atmospheric Cherenkov detector

*Corresponding author.

E-mail addresses: reposeur@in2p3.fr (T. Reposeur).

✠ Deceased.

PII: S0168-9002(02)01005-7

1. Introduction

The high energy ends of the spectra of some Active Galactic Nuclei and pulsars dominate their power output. Studying the γ-ray emission, especially in the context of measurements made over the entire electromagnetic spectrum, provides critical tests of our understanding of the structure of these objects and of the acceleration processes involved [1,2]. Measurements also give information on the extragalactic medium: γ-rays incident on near-infrared photons are absorbed, over cosmological distances, through electron–positron pair production. This phenomenon can produce source-distance dependent cutoffs in spectra in the GeV–TeV range, indirectly probing the infrared background [3].

Over the last decade, the study of the electromagnetic spectrum was extended into the low end of the GeV region by the EGRET satellite instrument which measured the spectra of nearly 300 point sources between 0.1 and 10 GeV [4,5]. In addition, it came to include very high energies from a few hundred GeV to beyond 10 TeV, through the use of *Atmospheric Cherenkov Telescopes* (*ACT*) [6–11], although only few sources have been detected so far. CELESTE aims to cover the energy range between EGRET and previous ACTs.

ACTs make use of the fact that the interaction of an incoming γ-ray with the atmosphere results in an electromagnetic shower whose e^+e^- pairs produce Cherenkov light. Below a few tens of TeV, the substantial information reaching the ground is the light, which is what ACTs detect. Two methods have been successfully used.

1.1. The imaging technique

An image of the shower is formed in a multipixel camera mounted on a single large mirror. Discrimination between γ-ray induced and hadron-induced showers is obtained from image shape analysis and directionality [12]. Several telescopes now operate all over the world [13–16] with energy thresholds between 250 GeV and 1 TeV.

1.2. The sampling technique

Pioneered by ASGAT [7] and THEMISTOCLE [8], this method uses multiple mirrors distributed over a surface comparable in size to that of the 200 m in diameter area illuminated by a shower. In general, each mirror has a single phototube associated with it, providing a sample at that point of the Cherenkov photon flux and the arrival time of the Cherenkov light wavefront.

Energies above 10 GeV are presently only accessible using ground-based ACTs, although ongoing satellite projects, notably GLAST [17], to be launched in 2006, and in a narrower energy range AGILE [18], scheduled for 2002, will have sufficient sensitive area to reach 50 GeV and beyond. In addition, the possibility for AMS in the International Space Station Alpha to detect γ-rays in 2003 is under study [19].

With a minimum energy threshold of 250 GeV, current ground-based imaging telescopes leave a window open in the energy range 10–250 GeV. Several projects aim to lower the energy threshold to 100 GeV or lower. CANGAROO3 [20], HESS [21] and VERITAS [22] will use arrays of several telescopes, while MAGIC [23] and MACE [24] will operate with a single very large (17 m diameter) mirror on a single mount. They will be brought into operation over the next few years.

In the meantime, the solar plant variant of the sampling technique is proving to be a good alternative to detect γ-rays in the 10–250 GeV energy gap before the next generation of satellites and imagers arrives. The use of existing solar installations provides a unique opportunity to open this particularly rich window rapidly and at a relatively low cost. Currently, STACEE [25], GRAAL [26] with a higher threshold, and CELESTE are in operation. A fourth telescope is under construction at the SOLAR-II plant [27].

In the next section we describe the wavefront sampling approach to γ-ray detection in the 50 GeV range. Sections 3–5 detail the CELESTE optical, electronic and data acquisition systems, respectively.

2. CELESTE: using a solar installation to reduce threshold

2.1. Design considerations

The minimum energy threshold of a Cherenkov telescope is limited by the rate of accidental triggers produced by the night-sky background light:

$$E_{\text{threshold}} \propto \sqrt{\frac{\Omega\tau\phi_{\text{nsl}}}{A\varepsilon}}$$

where Ω is the solid angle seen by the photodetector, τ the integration time necessary to collect the shower light and produce triggers, ϕ_{nsl} the photon flux of the night-sky background, A the light-collection area and ε the photon detection efficiency.

In the 30–300 GeV γ-ray range, the angular size of the induced electromagnetic shower as seen from the edge of the light pool is several milliradians which constrains the minimum solid angle Ω. Moreover, τ is in practice limited by the duration of the shower to a minimum of about 5 ns. The level ϕ_{nsl} of the night-sky light in the 330–550 nm range of interest here is roughly 1800 photons/ns/m^2/sr [28] for clear skies and an average background starfield. In the future, new photodetectors may lead to improved values of ε but currently photomultiplier tubes (PMTs) are universally used, with a typical efficiency in the 20% range. These general considerations single out the light-collection area parameter A as the most promising way to reduce threshold. For low detector threshold the counting rate due to atmospheric muons increases rapidly. These muons are easily rejected by requiring coincidences between heliostats separated by more than 15 m, and in this context the large collection area of solar plant mirrors comes to mind [29,30].

2.2. Making use of the THEMIS plant

Located near Font-Romeu in the French Pyrénées (42.50N, 1.97E, 1650 m a.s.l.) THEMIS, built and operated by Electricité de France (EDF) in the 1980s, had 200 54 m^2 in area heliostats. After it was shut down, the ASGAT [7] and THEMISTOCLE [8] experiments were built to explore, respectively the sub-TeV and the multi-TeV regions, taking advantage of the heliostat mountings and the general infrastructure, and in the mid-1990s the CAT high-resolution imager [14] was installed. However, re-use of the heliostat *mirrors* implies collecting the Cherenkov light near the point where the solar energy was focussed, close to the top of the 100 m THEMIS tower due south of the heliostat field. Consequently in 1995 the solar furnace was removed from the tower and replaced first by two 1.6 m in diameter secondary mirrors for feasibility studies with 6 heliostats [28], and then by the present secondary optics which can accommodate up to 90 heliostats.

2.3. Overview of the CELESTE detector

Until October, 2001, the experiment used forty of the 54 m^2 mirrors, chosen to have a uniform distribution over the 200 m $\times$ 300 m field (Fig. 1).[1] Typically the showers that trigger have a projected impact point $<$50–100 m from the center of the field, leading to an effective sensitive area in the 10,000 m^2 range. The secondary optics (Fig. 2) defines the field-of-view of the heliostats, equalizing it over the full heliostat-to-tower distance range of 3. In addition, the light detected by a given PMT is restricted to that from the appropriate heliostat with an undetectable cross-talk from its neighbors. The geometry of the setup associates a large collection area with a small solid angle resulting in a high, but tolerable, continuous background light flux on the PMTs.

After amplification, the PMT signals are split, with one of the two resulting channels digitized by flash ADCs (FADCs) clocked at 1 GHz. The other channel goes to a trigger system combining analog summing of the signals in 5 groups of 8 heliostats followed by a digital majority coincidence logic using the signals produced by the group discriminators. When a trigger occurs, the FADC data are

[1] Since October, 2001, we use 53 heliostats. Apart from the tracking, the additional heliostats have the very same features as the former ones.

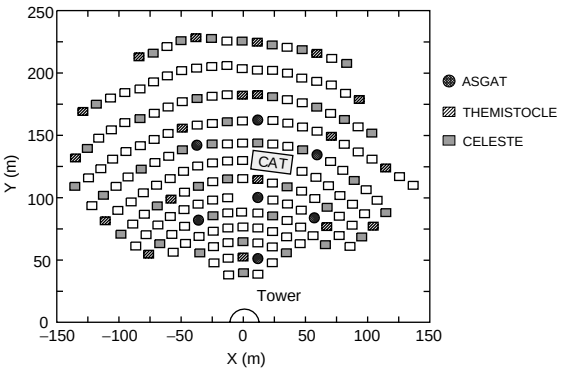

Fig. 1. Heliostat positions for the THEMIS solar plant. Of the three sampling experiments, CELESTE is the only one to use the original heliostat mirrors.

read out, and their subsequent off-line analysis provides accurate time values as well as information on the pulse shapes and amplitudes. A Global Positioning System (GPS) time is also recorded for each event. Weather conditions (temperature, humidity, pressure) and PMT currents are recorded during data taking, as is the Flash ADC clock frequency.

2.4. Data-taking and analysis considerations

For primary energies above 1 TeV, the Cherenkov light wavefront is conical and accurate timing is enough to reconstruct the direction of the incident γ-ray (Fig. 3). At lower energies, however, the wavefront becomes essentially spherical and the determination of the incident angle requires reconstructing two points: the center of the sphere using the arrival times, and the impact point using the pulse heights.

Fig. 4 illustrates the characteristics of the light pool on the ground for a typical γ-ray shower ($E_\gamma = 40$ GeV) and a proton shower ($E_p = 150$ GeV). Different energies were chosen here in order to have the same amount of Cherenkov light at the heliostat level, since below a few TeV a proton tends to be less efficient than a γ-ray in producing Cherenkov light due to the rapid energy degradation that occurs in the initial hadronic cascades. The electronic sub-showers, once produced, are of lower average energy and the particle energies fall below the threshold for producing Cherenkov radiation sooner. For γ-ray showers one clearly sees a disk-like structure with a ring of higher density at a radius of about 130 m; this

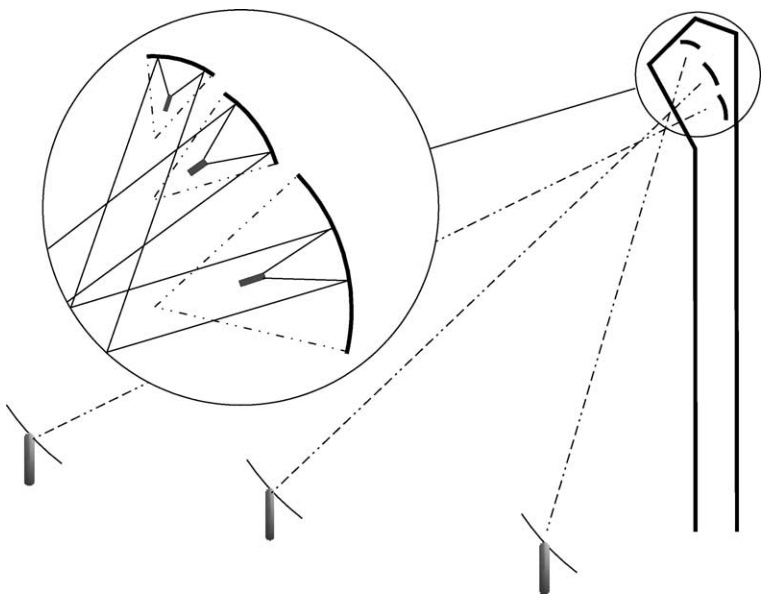

Fig. 2. Secondary optics: the light from a given heliostat reaches only one phototube.

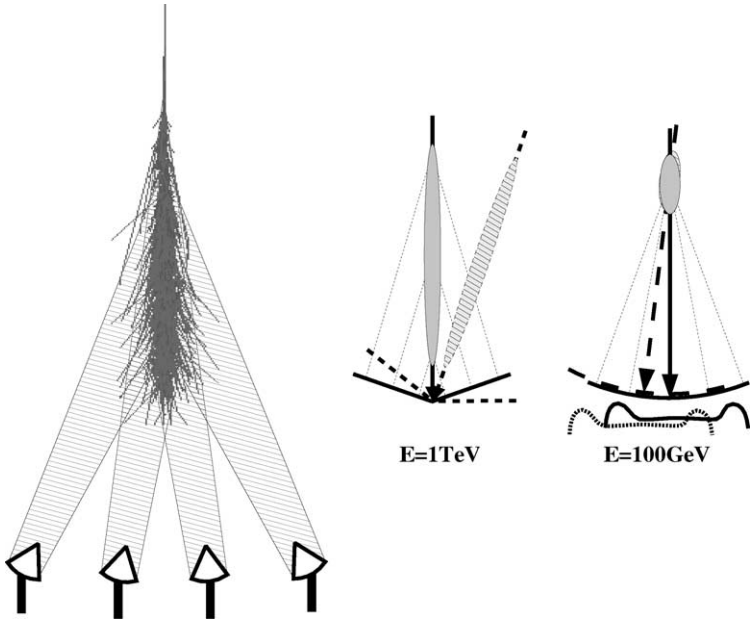

Fig. 3. The principle of the sampling method (see text).

value turns out to be independent of the γ-ray energy in our energy range. The structure varies much more in the case of protons mainly because of the angular and energy dispersion of the massive particles produced in the first stages of the shower. Moreover, this dispersion induces larger multiple scattering effects. Finally we note that the 150 GeV proton shown would not trigger the experiment because of its large arrival time dispersion (see Section 4.3).

Fig. 5 shows the average Cherenkov photon density within a 10 mr field-of-view for a 30 GeV γ-ray and two different pointing strategies, *convergent pointing*, where the heliostats reflect light from a region above the field at an altitude chosen to be close to the shower maximum, and *parallel pointing* with the heliostats aimed to see the astronomical source at infinity. For an array of the size of THEMIS, the density distribution obtained with parallel pointing allows for a better determination of the impact parameter of the shower, while convergent pointing maximizes the total number of collected photons, and therefore minimizes the energy threshold for reasonably well-centered showers. For our first data sets we chose convergent pointing, using the observed light distribution to reconstruct the shower impact parameter. More recently a "mixed pointing" strategy [31,32] has most often been used, in which half of the heliostats form a group converging to 11 km in altitude and the others to 25 km.

Extracting a signal requires comparison between observations of a potential γ-ray source (ON-source) and a background control region offset in right ascension from the ON-source position (OFF-source). The task is complicated by subtle triggering effects induced by variations in the extremely high background light level (see Section 4.3). In the analysis process, a software padding technique [33,34] is used to equalize noise levels in the ON and OFF data samples. The application of such a procedure takes advantage of the fact that the experiment is fully simulated, from shower development to the output of the electronics. The γ-ray interaction is reproduced using the KASCADE code [35]. Each Cherenkov photon is then followed through the optics to the photocathode of the PM tubes. Finally, the electronics response is simulated. Careful attention is paid to the latter because of the precise timing needed in the

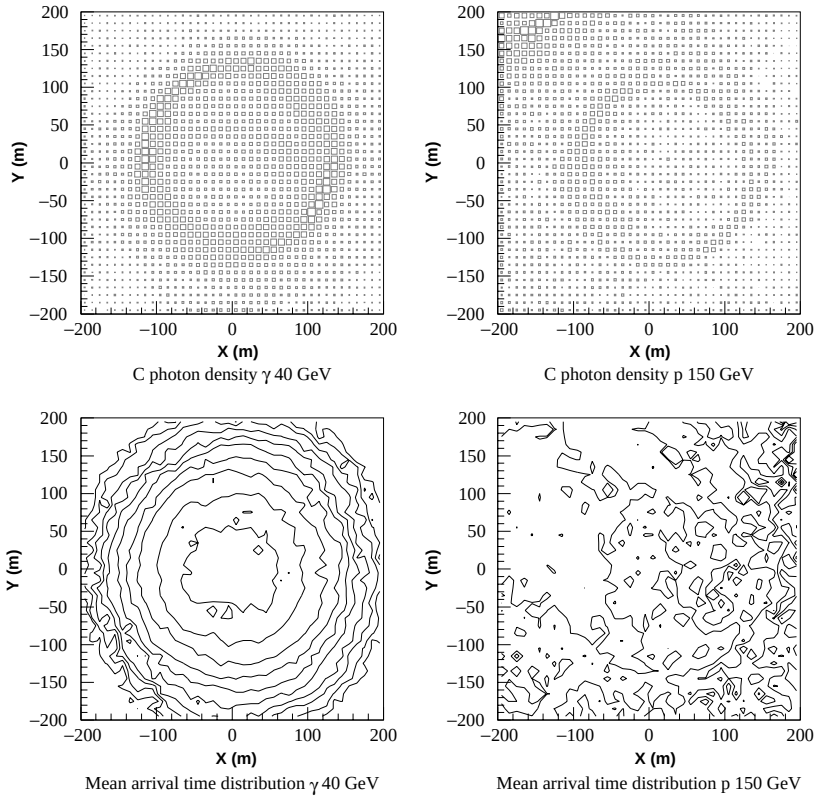

Fig. 4. A γ-ray shower (40 GeV, left), and a proton shower (150 GeV, right). Top: Cherenkov photon density on the ground relative to the extrapolated impact point of the primary particle. Bottom: Cherenkov arrival times for 10 m × 10 m bins.

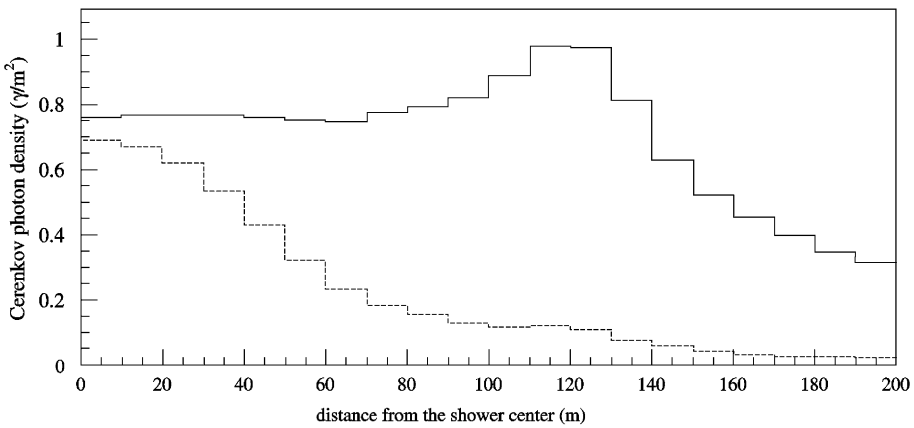

Fig. 5. Calculated average Cherenkov photon density (γ/m^2) for vertical 30 GeV electromagnetic shower, versus distance from the shower center in meters. The solid (dashed) histogram is for convergent (parallel) viewing with a 10 mr field-of-view.

analysis. A full description of the simulation can be found in Ref. [31]. More details on the analysis procedure can be found in Ref. [33].

3. Optics

3.1. Heliostats

Fig. 6 shows a single heliostat which consists of 8 modules, each having 6 elementary mirrors measuring 60 cm × 181 cm. An additional central module has two 256 cm × 41 cm panels. Each is made of a 2 mm thick back-silvered glass layer glued to a 5 mm thick sheet of float glass. The panels are supported at 60 cm intervals using shims that produce a slightly curved cylindrical surface corresponding to the desired focal length. When the modules were assembled, the panels were oriented so as to obtain this same focal length, as was the case when the 8 modules were mounted on the heliostat structure. The focal length category for a particular heliostat was chosen to correspond to its distance from the tower. Table 1 gives the overall properties of the heliostats. It should be noted in addition that the reflectivity falls steeply around 330 nm, in part due to the glass front surface, so the UV part of the spectrum is cut off.

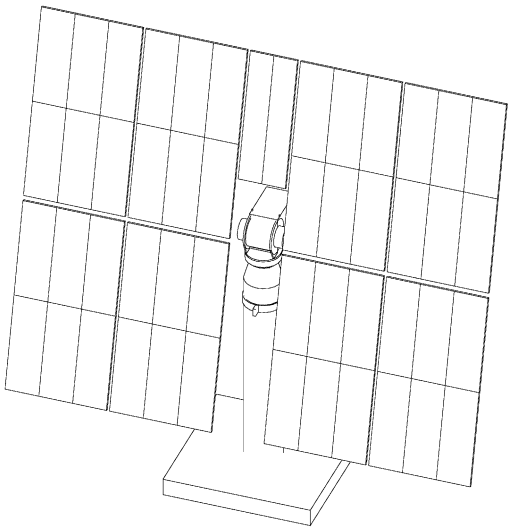

Fig. 6. View of a single heliostat.

Table 1
Heliostat properties

Size (m^2)	7.34×8.84
Reflector area (m^2)	54
Focal length (m)	100, 140, 200, or 240
Reflectivity (%)	90 at 400 nm
Pointing accuracy (deg)	$\ll 0.1$

In spite of the fact that the heliostats had been left unused for over 10 years, it was possible to put them back into operation, often with only minor component-replacement work. This included the on-board microprocessor system controlling the two DC motors of the alt-azimuth mounting. Replacement parts could be obtained, except for the microprocessor chip itself for which the original THEMIS stock is sufficient for a 40 heliostat array to run for several years. In the field, some sections of the control cabling had deteriorated and required replacement. (The 13 heliostats added in October 2001 are now being brought into operation, with a newly developed, radio-controlled electronic system.)

The heliostats now receive their pointing instructions from a central PC computer in the tower near the secondary optics via a differential transmission link, followed by signal conversion in the field to the standards of the original EDF current loop system. The software was developed from that of the THEMISTOCLE experiment and is used both by CELESTE and CAT. The pointing step is 0.14 mrad. A source moves in the sky with an angular velocity corresponding to at most 1 step every 2 s, and the 10 s necessary to send pointing coordinates to the 40 heliostats gives an uncertainty of 0.7 mrad which is far less than the measured angular resolution of the telescope.

In order to verify the quality of the pointing, we monitor the phototube anode current while following a star, introducing small corrections in the pointing direction so as to scan around its nominal position. Fig. 7 shows the result for η Her for one heliostat. The plot is 14 mrad wide in both directions and indicates that the pointing accuracy is satisfactory considering the field-of-view of the

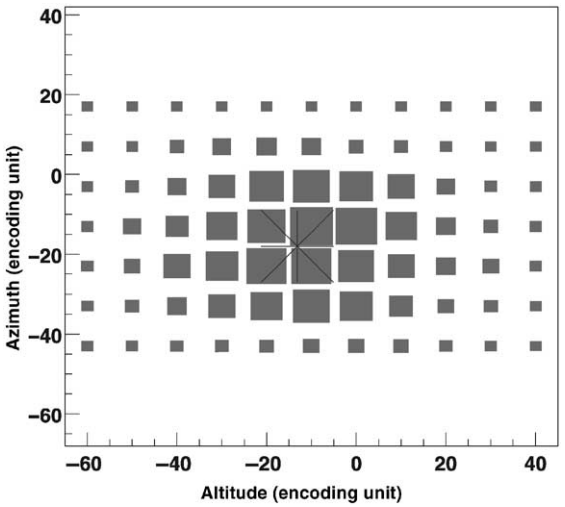

Fig. 7. Phototube anode current versus altitude and azimuth (in encoding units) relative to the nominal star position. Histograms are 14 mrad wide in both directions. The axis origins correspond to the hardware zero value of the coding system and are arbitrary.

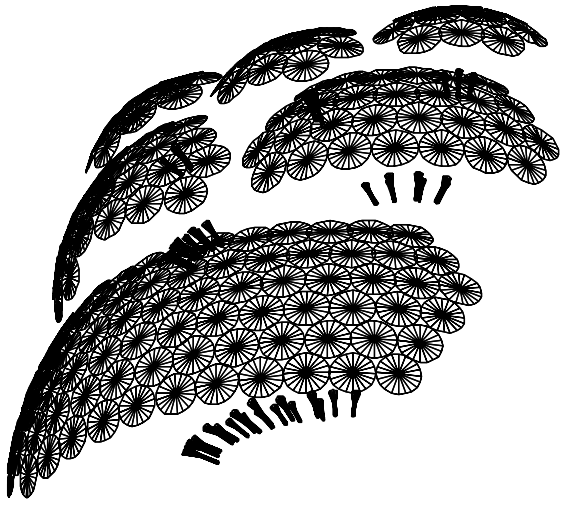

Fig. 8. Secondary optics of CELESTE, showing the three groups of spherical mirrors (see text). The PMTs with their associated cones are also shown.

telescope. The center of the distribution may vary slightly as an object is followed over the sky, but it always stays well within the 10 mrad field-of-view of CELESTE. The accuracy of the pointing is further confirmed by the detection of γ-rays from the Crab Nebula, the detection of the optical component of the Crab pulsar, and the presence of common γ-ray events with the CAT detector; all of these exclude significant pointing errors [33]. This technique of "scanning stars" is periodically used in order to check the pointing quality over the observations periods.

3.2. Secondary optics

A solar plant delivers the light collected by the different heliostats to a common receiver, while a Cherenkov sampling telescope needs to obtain separate information from each primary mirror, requiring a secondary reflection system (Fig. 2). The secondary optics of CELESTE consists of three groups of composite spherical mirrors with focal lengths of 1.8, 1.1 and 0.65 m directed toward heliostats located at the far, middle and near parts of the field, respectively (Fig. 8). The circular borosilicate-glass mirror elements are 50 cm in diameter and 11 mm thick, with front-surface aluminization protected by a SiO_2 layer. These elements overlap slightly to reduce gap losses to $<10\%$.

We have adopted on-axis optics (Fig. 9) which provides good field-of-view definition and small cross-talk, but induces a loss in the light-collection efficiency due to shadowing by the cameras (PMT blocks). This is estimated from simulation to be 20–30% [31]. Off-axis optics gives better light transmission but with bigger cross-talk and less well defined fields of view.

3.3. Winston cones

The field-of-view is defined by Winston cones glued to the phototubes. A Winston cone [36] is an optical device with a revolution symmetry axis whose contour is generated from a parabola. A characteristic angle θ defines the parabola's focal length by $f = \Phi_e \sin(\theta)(\sin(\theta) + 1)/2$ where Φ_e is the entrance diameter of the cone. The relationship between the entrance and exit diameters is given by $\Phi_s = \Phi_e \sin(\theta)$ and the height of the cone is $h = f \cos(\theta)/\sin^2(\theta)$. The incident light rays that can

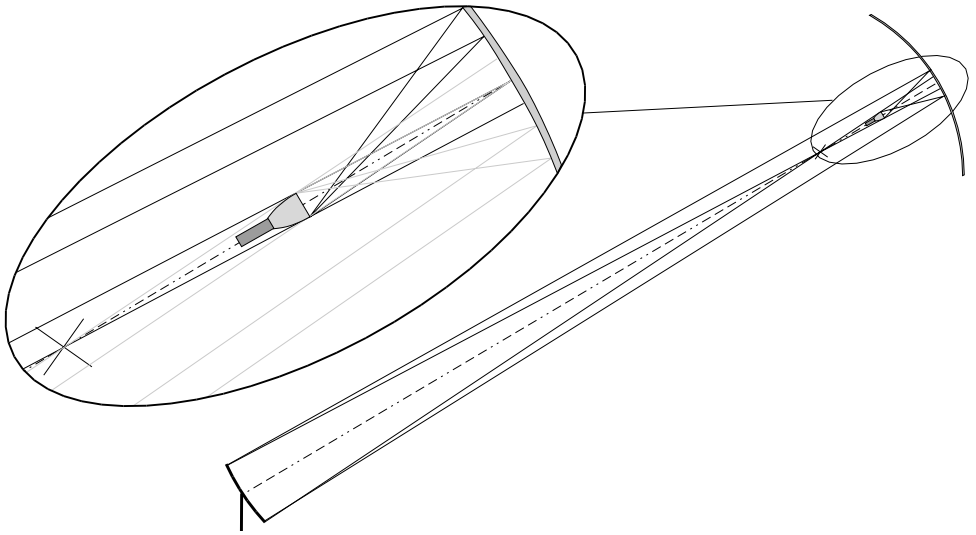

Fig. 9. Schematic of an "on-axis" secondary optics. Each phototube sees a single heliostat defined by the entrance window of the Winston cone. Note the shadow from cone-phototubes assembly.

exit the cone are those with an angle in the $0-\theta$ range with respect to the symmetry axis of the cone. The entrance surface of the cone is positioned to receive the image of the heliostat formed by the secondary mirror. Thus we limit the part of the secondary mirror "seen" by a particular phototube to a zone of 10 mrad angular diameter viewed from the heliostat. This limitation also ensures that light from the environment of the heliostat (objects on the ground and also neighboring heliostats) which reaches the cone as a result of spherical aberration after having been reflected from other parts of the same secondary mirror does not reach the photocathode. Fig. 10 shows the principle of a Winston cone and the angular acceptance as a function of the photon incident angle.

In principle, the exit diameter of the cone should simply be made equal to the photocathode diameter. In practice, the photocathode has some curvature which causes losses at the interface. This problem was solved by shortening the cone and therefore virtually moving its exit surface into the phototube. Fig. 11 shows the results before (dotted line) and after (solid line) this modification.

The cones are all made of FK5-487704 glass from Schott. Their absorption is 1% or less for a 2.5 cm length in the 350–800 nm wavelength range, with an optical index varying from 1.5 to 1.48, close to that of the photocathode.

4. Photomultiplier tubes and electronics

Fig. 12 gives a schematic overview of the electronics. We will detail the different parts of this apparatus in the next sections.

4.1. Photomultipliers

Very accurate timing is the key to correct reconstruction of the wavefront of the Cherenkov light. The XP2282B 8-stage photomultiplier tube from Philips is well suited to our purpose with the following characteristics:

- Entrance window: Borosilicate glass,
- Photocathode sensitivity: 300–650 nm,
- FWHM single photoelectron pulse: 2.2 ns,
- Optical index of the photocathode: $\simeq 1.48$ (close to that of the Winston cones).

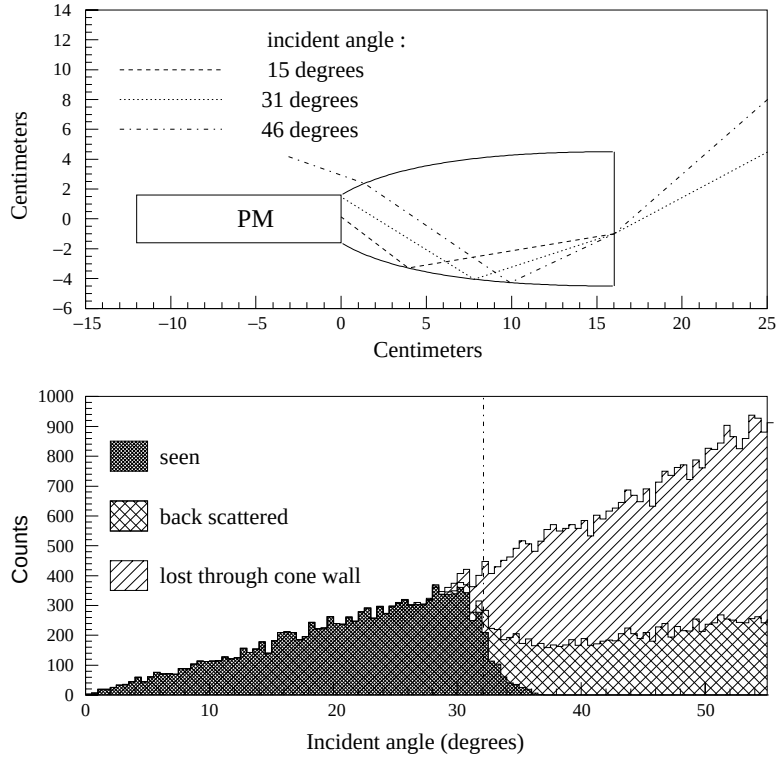

Fig. 10. Geometry of a Winston cone, and the associated response as obtained from Monte Carlo simulation. Function of the incident angle of the photons.

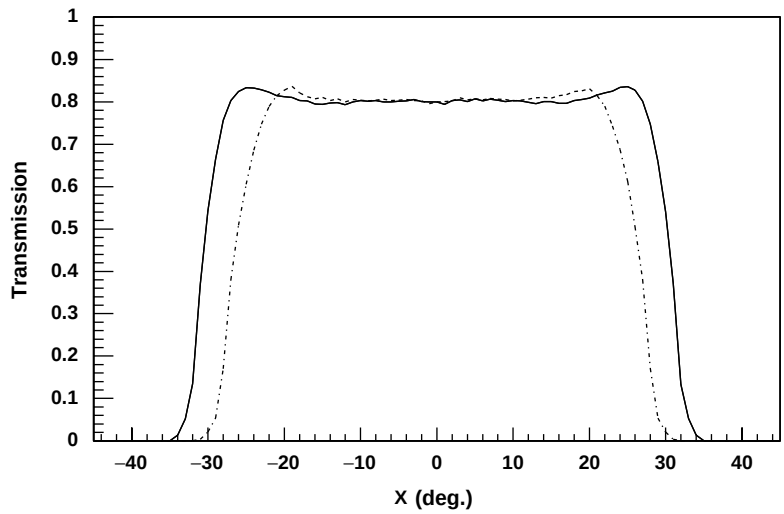

Fig. 11. Optical transmission of the cone-photocathode interface as a function of the incident angle (in degrees) on the entrance window. The dotted line corresponds to the initial cones and the solid line to the truncated cones.

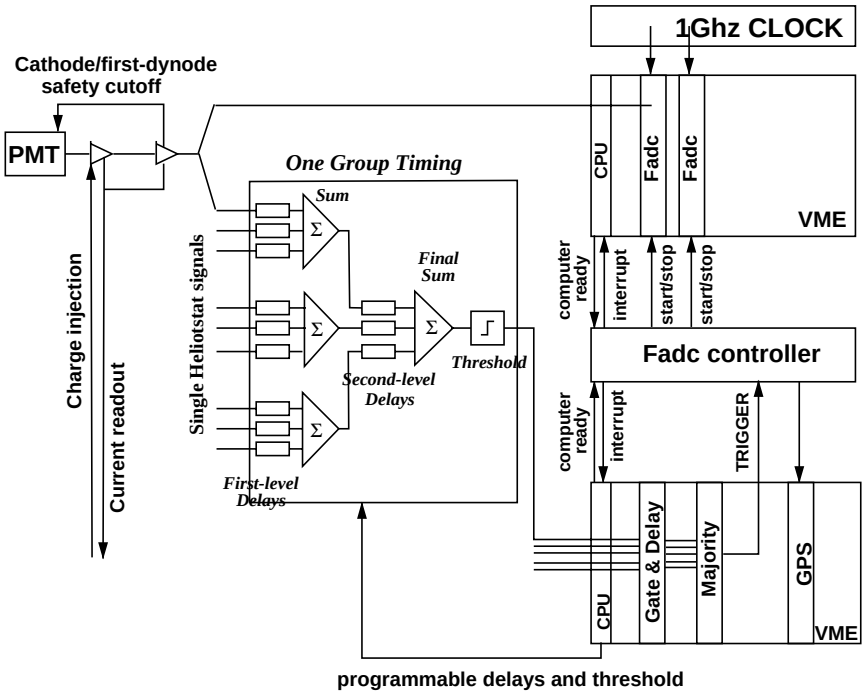

Fig. 12. Schematic diagram of the CELESTE electronics.

Special tube bases were developed for the experiment. The cathode to first dynode voltage is fixed at a relatively high value, 520 V, in order to minimize fluctuations and therefore improve the time resolution. To prevent damage to the tube, when the anode current exceeds 40 μA this voltage is switched off rapidly and replaced by 20 V of reverse bias, reducing the overall gain by a factor of roughly 1000. The residual sensitivity can be explained by photoemission from the first dynode. The remaining voltage is approximately equally distributed over the 7 other stages, the last two being transistor-stabilized. The total voltage is typically 1200 V for a PMT gain of 5×10^4, kept low to limit the DC anode current from the night-sky light to less than around 10 μA. This low gain is compensated for in the tube base using an INA10386 $\times 25$ amplifier having a 1.5 GHz bandwidth.

A further $\times 5$ gain is provided in modules located close to the secondary optics. These also include fan-outs for test signal charge injection at the PMT anode level and circuitry to monitor the anode currents and implement the rapid first-stage voltage cutoff. The anode currents are digitized and recorded using a PC; the data are stored for off-line use. The signals reach the counting house after a total of 25 m of RG-58 coaxial cable and the pulse widths are slightly under 5 ns FWHM.

4.2. Phototube calibration

The first step in the energy calibration of the detector is the knowledge of the relationship between the output voltage of the PMTs and the number of photoelectrons (pe) on the photocathode. We have calibrated the PMTs using the *single photoelectron* technique. We illuminate them in situ with a low visible light flux and extract the single photoelectron spectrum for each of a set of high voltages using a variable-threshold discriminator and a scaler. Fig. 13 shows the result for one channel and nine high-voltage values.

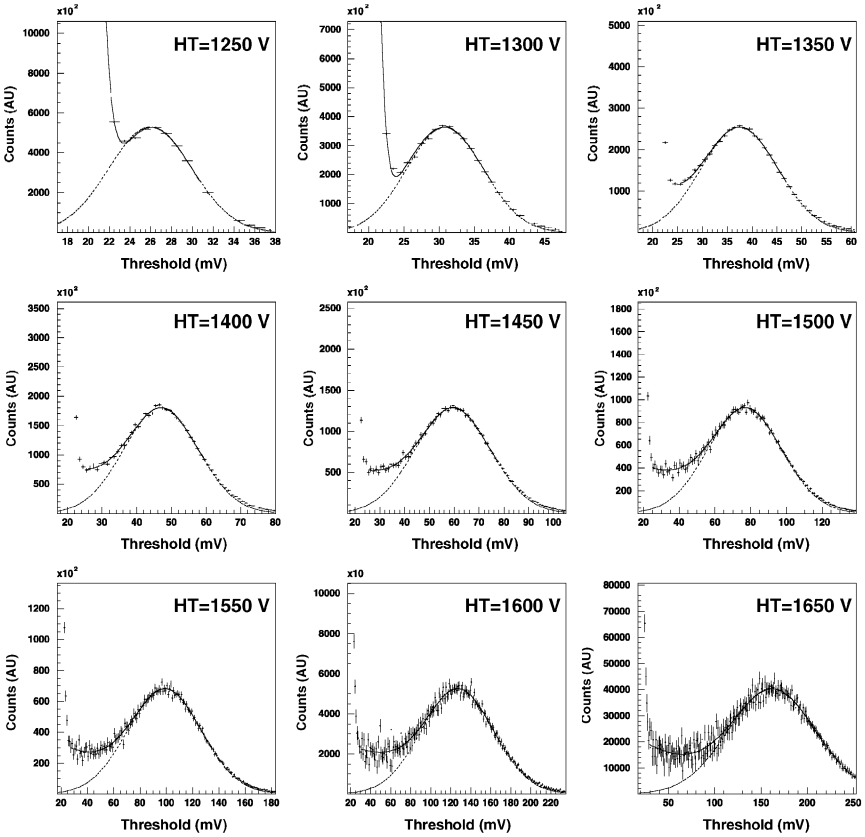

Fig. 13. Single photoelectron spectra for one typical channel and several high voltages.

Because of the large night-sky light flux and since we wish to run the PMTs well below the recommended maximum anode current of 200 μA, we have chosen a gain of $\approx 5 \times 10^4$ giving a sensitivity of 10 mV/pe on the average at the input to the acquisition and trigger electronics in the counting house, and after amplification. For most of the 40 phototubes it has been possible to measure the single photoelectron peak down to 10 mV; to complete our calibration for the few others we extrapolate down to 10 mV per photoelectron using the following function:

$$f(V) = 10\ \text{mV} \times \left(\frac{V - 520}{p_0 - 520}\right)^{p_1}$$

where 520 corresponds to the fixed cathode to first dynode voltage. Typical values for p_0 and p_1 are 1250 V and 6.5, respectively. Fig. 14 shows the result of this fit. Thus the PMT gains can be adjusted to obtain 10 mV/pe. In practice, however, the final gain values used also take into consideration *relative heliostat efficiency* as determined through measurements of the hadronic shower charge spectra using the FADCs, combined with results of simulations. This subject, closely related to the question of energy calibration, will not be treated in this paper.

4.3. Trigger

The goal of the experiment is to have as low an energy threshold as possible, but at $E_\gamma = 30$ GeV, for example, the mean number of Cherenkov photoelectrons per heliostat is only 3. This must be

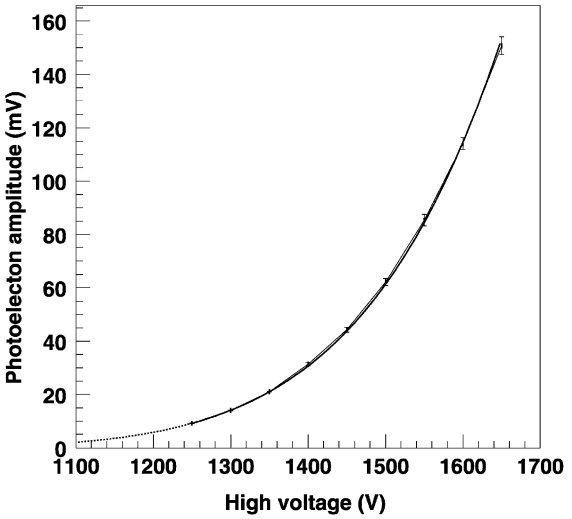

Fig. 14. The solid line is the fit of the single pe peak positions after pedestal subtraction, the dashed line is the extrapolation. Same channel as for Fig. 13.

compared to the night-sky background which gives a mean value of 1 and 0.7 pe/heliostat/ns in the Crab direction and zenith, respectively. For a trigger, a pure analog sum of the signals of all the heliostats would maximize the ratio of signal to background fluctuations. At first sight this might appear to be the best solution. However, such a trigger would be very sensitive to local muons and large amplitude after-pulses from the PMTs.

Instead, we have chosen a *hybrid analog-logic* trigger in which we first sum 8 heliostats at the analog level, applying a threshold to the resulting signal. A majority decision is then taken submitting the five discriminator output signals to a CAEN V495 majority logic module using a coincidence width of 10 ns. This method takes advantage of the increased signal/background ratio while the muons and after-pulses are rejected by the group coincidence requirement.

Since the source being observed is continuously moving across the sky, the relative arrival times of the shower light on the heliostats are constantly changing, and it is necessary to compensate for this in the trigger system. The maximum angular velocity of an object in the sky is 15°/h, so the delay variation between two distant heliostats (200 m) is at most $\simeq 1.5$ ns/min; a delay correction increment of 1 ns is used, computed every 30 s, sent to the electronics, and also recorded by the acquisition system.

A specially designed module (see the central part of Fig. 12, labelled "One group timing"), one per group, adjusts the relative delays during data taking and also performs the summing. For each heliostat a fixed delay accounts firstly for the different arrival times at the heliostats, calculated for the wavefront of a source located at the zenith, and secondly for the path differences from each heliostat to the secondary optics. Then the variable delay corresponding to the actual source position is performed in two stages, first individually for each heliostat and then on an intermediate signal obtained by summing a group of three. (The module has 9 inputs of which only 8 are currently used.) The total delay range obtainable is 254 ns. To compensate for the varying cable attenuation, when a length of cable is removed it is replaced by the appropriate fixed attenuator. This system receives its commands via an RS 232 serial link.

To obtain the final trigger, the 5 logic outputs of the delay module discriminator are put in time by a CAEN V486 programmable delay circuit with a 500 ns range. Its deadtime, roughly 1.5 times the delay value, currently limits the minimum threshold that can be applied with the discriminator. However, we have developed a delay circuit with a deadtime of only $\simeq 20$ ns which will accept the higher rates incurred when lower threshold settings are used. It should be noted that the limited range of the programmable delays restricts the observable part of the sky to within 30° of zenith but this is of little importance since the heliostats optical losses increase for sources far from the transit.

We want to emphasize the muon rejection power of this trigger. By requiring several (typically 3) groups of 8 heliostats for a trigger, we select only the showers which illuminate a large fraction of the field. Muons from hadron-induced showers only produce significant Cherenkov light close to the ground and the spatial extension of their light pool is <20 m, making it impossible for them to trigger. This result is confirmed by studying common events with the CAT imager [14], which is very sensitive to muons. CAT events

re-triggered with CELESTE show a dramatic suppression of muons [31,37].

4.4. Trigger performance

As indicated in Section 2.1, the main limitation encountered when attempting to lower the energy threshold comes from the accidental coincidences produced by the night-sky background light. Their rate changes with the pointing direction (stars in the particular field of view, zones of the sky affected by urban light pollution, etc.) and from night to night (relative humidity, snow covering the ground, etc.). We check the threshold for each observation of a source using a measurement of the trigger rate as a function of this threshold. Fig. 15 shows a typical trigger rate curve recorded while following the BL Lac object 1ES2344+514 and using convergent pointing. The steeply rising portion at low threshold is caused by the accidental coincidences from the night-sky light fluctuations. The flat decrease at high threshold corresponds to cosmic rays and in fact these triggers disappear when the timing between the groups is incorrect. The threshold value adopted lies in the region where the rate of night-sky background triggers has been reduced to $<1\%$. For most observations its value is in the range 4–4.5 pe/heliostat and the corresponding trigger rate is about 20 Hz.

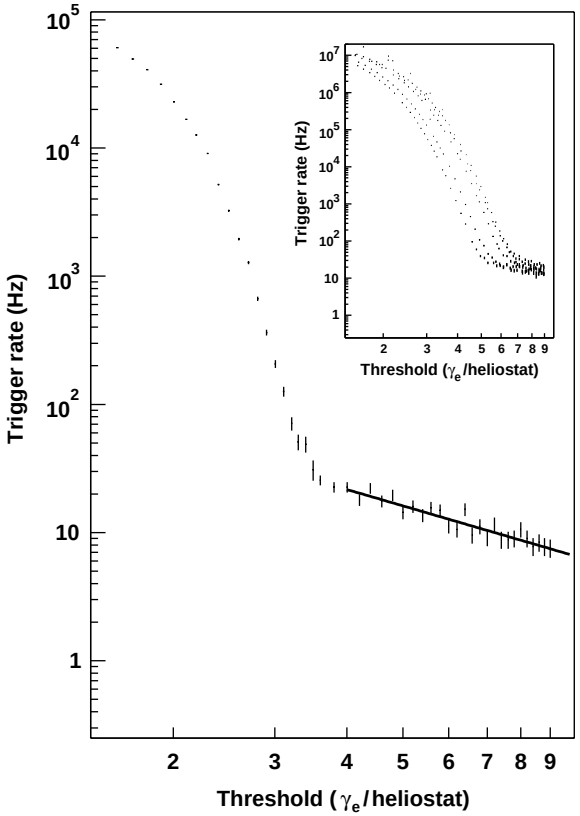

Fig. 15. Trigger rate as a function of threshold in photoelectrons/heliostat for a "3 groups out of 5" majority coincidence.

The inset of Fig. 15 shows the counting rate for the five individual groups. The differences in rate from one group to another mainly come from the slightly different parts of the sky seen by the heliostats leading to small differences in the night-sky background, as well as to the residual attenuation in the switched cable delay modules. The night-sky light clearly dominates below 7 pe/heliostat; above that value the rate levels off at $\simeq 10$ Hz.

To investigate this behavior further, we have performed the same experiment by illuminating the phototubes in order to reproduce the anode currents observed in the 1ES2344+514 measurement, the front door of the tower being closed. Fig. 16 (bottom) shows the rates for each of the five groups. They look very similar to those of the inset of Fig. 15. We interpret the flattening of the curves at high threshold as being due to muons passing through the Winston cones with sufficient light output to trigger a single group at a rate of about 1 Hz per channel, i.e. 8 Hz per group. Once a coincidence is required (upper part of Fig. 16, in this case between 4 groups out of 5), the flat part of the curve vanishes as expected due to the absence of showers. The final trigger rate stays below 1 Hz for a threshold >4 pe/heliostat so we can conclude that accidental coincidences are negligible in an ON–OFF analysis procedure.

4.5. Digitization

Timing being a key requirement for the analysis, we chose to digitize at a 1 GHz rate. In this way both time and amplitude information is available

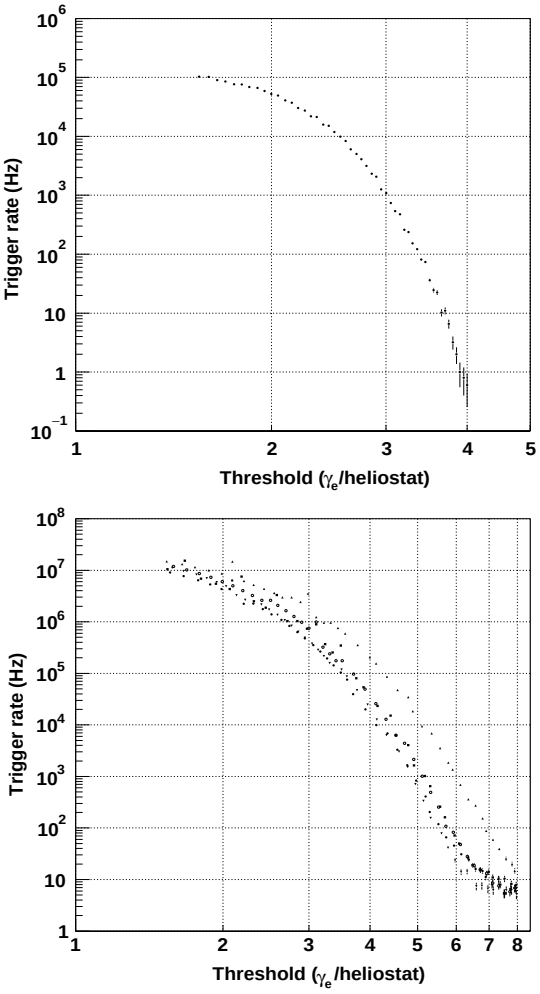

Fig. 16. Trigger rate as a function of threshold in photoelectrons/heliostat. Case of "Heliostat field OFF" (see text). Top: multiplicity 4/5 coincidences. Bottom: individual group rates.

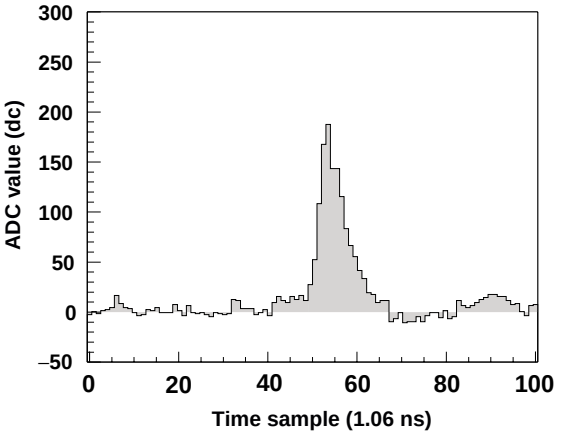

Fig. 17. Typical Cherenkov signal in the flash ADC, after pedestal subtraction, in digital counts versus time samples (1.06 ns). One photoelectron is approximately 3 DC.

from the readout channel, even for channels which would not have participated in a more conventional *discriminator+TDC* setup. The two-channel ETEP 301C module used was specially developed for CELESTE [38]. It is clocked at 940 MHz with a circuit also specifically developed for our needs and now available from ETEP [38].

Capacitive coupling the DC component of the signal, and since the 8-bit FADC is unipolar (0–−2 V), a voltage offset of −0.25 V is introduced to ensure that positive fluctuations and overshoots will be recorded.

The digitized data are stored continuously in an 8-bit memory 2048 words deep. Due to speed limitations, eight 125 MHz memory circuits are used in parallel, receiving the data via a fast multiplexer. When a trigger occurs, the encoding is stopped and the memory is made available for readout. An internal register locks the memory address when the stop signal is received, and this makes it possible to calculate, channel-by-channel, the address of the zone in memory where the signal is expected, based on the nominal arrival time of an on-axis shower incident on the center of the heliostat field. The Cherenkov readout is limited to a 100-sample window centered on that point. Fig. 17 shows a typical signal recorded by the ETEP 301C.

As mentioned in Section 2.4, the arrival times of the signal are used to reconstruct the interaction point of the γ-ray in the atmosphere. The accuracy of this position measurement depends directly on the precision of the time values used and therefore requires knowledge of the various signal delays leading to the digitizer. A database contains all the relevant delay values for the cables and the electronics modules. This database is used by the main control computer to access the relevant

words in the FADC memories and also for the off-line analysis.

A measurement of the timing quality has been performed using a nitrogen laser ($\lambda = 337$ nm) installed for THEMISTOCLE which illuminates the whole field through a diffuser located near the top of the tower. The light pulse width is comparable to that of a Cherenkov signal. The positions of the diffuser, heliostat and secondary-optics elements are precisely known so the relative arrival times of the light pulses at the photocathodes can be calculated accurately.

For each channel and laser pulse, the pulse positions in the FADCs are obtained by fitting the pulse shapes; the mean values for a large number of laser pulses are then compared to the calculated arrival times. This provides a residuals histogram for the 40 channels as shown in the upper histogram of Fig. 18. The standard deviation of these values is σ of 1.5 ns, reflecting systematic errors in the delay values used. We then introduce channel-by-channel corrections in the database using these residuals. The bottom part of Fig. 18 shows the result of a different laser run making use of this correction. The dispersion is much better, going down to 0.4 ns.

The trigger is asynchronous with the FADC clock. When the trigger occurs close in time to a clock pulse the stop value that is recorded can differ by one count between two channels, giving a ± 1.06 ns from one channel to another for a particular event. The top histogram of Fig. 19 shows this difference for two typical channels. The data are obtained using the charge injection test signal sent to the phototube bases (see Section 4.1).

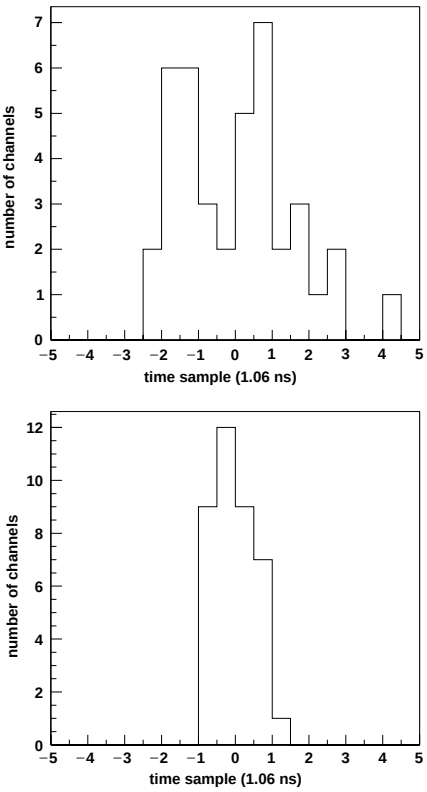

Fig. 18. Residuals of the arrival times for a laser run and for the 40 FADC channels, before and after corrections.

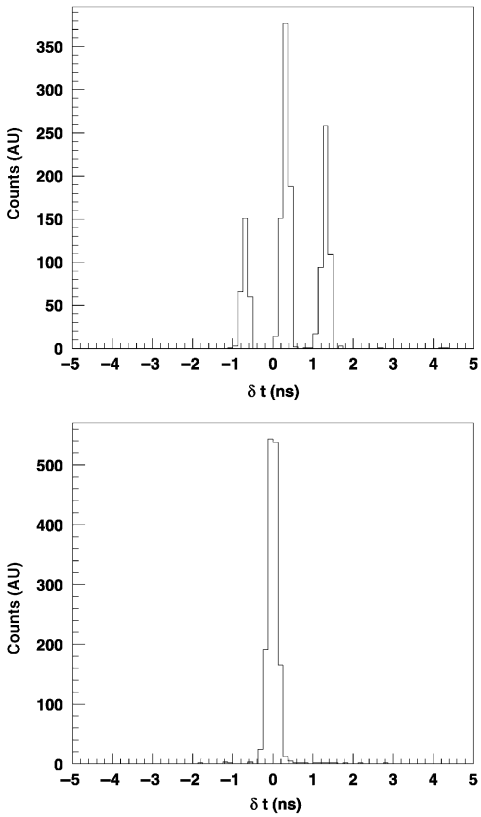

Fig. 19. Time difference between two channels in a charge injection run (see text). Top: raw data. Bottom: after correction using fiducial peaks.

This effect concerns of course the Cherenkov shower data as well.

The solution used to improve the synchronization between channels was to implement a *fiducial peak* in the data. When a trigger occurs, a test signal is sent out and after an additional delay the stop signal is sent to the FADCs. By reading out an additional sample of 28 ns, both the Cherenkov and the charge injection signals are available in the data. In this way we have an event-by-event time reference in each channel. The bottom part of Fig. 19 shows another charge injection run making use of the correction from the fiducial peaks. This reduces the time dispersion inherent in the electronics to the $\sigma = 0.15$–0.20 ns level. We want to emphasize the charge injection technique which allows a control of the experiment; each night of observation begins with such a run in order to check all the FADCs' channels and the acquisition system.

The FADCs have been calibrated in amplitude by encoding a signal of 5 ns FWHM which was itself calibrated with a Tektronix TDS620B oscilloscope. We found a small dependence (3%) on the pulse shape. A one photoelectron pulse corresponds to about 3 digital counts (DC), for a full range of 256 DC including the $\simeq 30$ DC offset mentioned above. The measured variation was within 20% for the 40 channels and is corrected for in the data analysis.

5. Data acquisition and system monitoring

The acquisition is organized on a client–server basis with the same architecture as for the CAT telescope [14]. A master HP-UX workstation running LabView code starts all the processes, each one on a dedicated platform. Using this scheme is natural because of the relatively large number of tasks and control operations to perform. Moreover, this allows for the addition of new clients when needed. All data transfers between computers use standard TCP/IP protocol.

The clients presently used perform:

- control and pointing of the heliostats (PC),
- phototube current readout (PC),
- weather data acquisition (PC),
- High voltage power supply control (LeCroy HV system),
- FADC and GPS readout, trigger control, scalers readout (3 VME crates).

The PCs run with MS-Windows 98 while the three VME crates each have a Motorola MVME162/172 68xxx processor board running the LynxOS v3.1 real-time system. Two of the crates contain only FADC modules while the third is used to control the trigger system, and read scaler, a GPS clock and a frequency meter to monitor the 940 MHz FADC. During data taking, all the calculations (e.g. trigger delays, pointing coordinates) are performed by the master machine then sent to the concerned client. Data are also collected by the master process which writes the data files to disk. The total acquisition time is approximately 7 ms, mainly due to the FADC readout, leading to a 20% deadtime at 20 Hz counting rate. This turns out to be very stable for a given set of observing conditions and is therefore easily corrected for in the analysis using scaler information.

One major concern is the stability of the experiment and the monitoring during data taking. In this spirit, several procedures are in places, which we want to summarize.

The accuracy of the heliostats pointing is periodically checked with the "star scan" procedure as described in Section 3.1.

Before every night we check that the electronics/data acquisition chain is working properly by a "charge injection" run with the setup described in Section 4.5.

Since the threshold may change with atmospheric conditions as well as with the sky region where the telescope is pointed, its value is checked by making a "trigrate" for each observed source (Fig. 15).

During data taking, several parameters are recorded:

- the PM tubes' high voltages and their anode currents are readout every 15 s,
- the heliostats' coordinates are readout every 30 s,
- the digitization clock frequency is recorded,

- in addition to the individual FADC channels, the analog signals from the trigger groups are digitized, allowing trigger control in the software analysis,
- the scalers record the trigger rate, the group rates,
- the weather parameters (temperature, dew point, pressure, humidity, wind) are recorded.

Finally, an on-line event display procedure is used to sample the data flow and check the data quality.

6. Conclusion

We have described the CELESTE atmospheric Cherenkov detector currently in operation at the THEMIS site in the French Pyrenees. CELESTE takes advantage of the large heliostat reflecting surface available combined with specially designed secondary optics in the THEMIS tower to make possible wavefront sampling at 40 points distributed over the 200 m $\times$ 300 m field. The electronic system was devised for accurate time measurements on signals superimposed on a high background noise level, and it provides triggering at a threshold between 4 and 4.5 photoelectrons per heliostat.

Results from data taken during the 1999–2000 winter period indicate clear detection, for the first time, of both the Crab nebula [33] and the Active Galactic Nucleus Mkn421 [31,39,40] with an energy threshold close to 50 GeV. This validates the CELESTE design described in the present paper and opens prospects for beginning systematic exploration of this region of the γ-ray spectrum in the near future.

Acknowledgements

Dr. L. Rob thanks the Ministry of Education of the Czech Republic for its financial support under grant LN00A006. Funding was also provided by the CNRS/IN2P3, the CNRS/INSU, the Bordeaux University, the Ecole Polytechnique and the Regional Councils of Aquitaine and Languedoc-Roussillon.

References

[1] C. von Montigny, et al., Astrophys. J. 440 (1995) 525.
[2] D.J. Thompson, et al., Astrophys. J. 465 (1996) 385.
[3] F.W. Stecker, O.C. De Jager, M.H. Salamon, Astrophs. J. 390 (1992) L49.
[4] D.J. Thompson, et al., Astrophys. J. Suppl. 101 (1995) 259.
[5] R.C. Hartman, et al., Astrophys. J. Suppl. 123 (1999) 79; D.J. Macomb, N. Gehrels, Astrophys. J. Suppl. 120 (1999) 335.
[6] J. Quinn, et al., Astrophys. J. Lett. 456 (1996) 83.
[7] P. Goret, et al., Astron. Astrophys. 270 (1993) 401.
[8] P. Baillon, et al., Astropart. Phys. 1 (1993) 341.
[9] R.J. Protheroe, et al., in: Highlights of the XXVth International Cosmic Ray Conference, Durban, 1997.
[10] R.A. Ong, Phys. Rep. 71 (1998) 93.
[11] C.M. Hoffman, et al., Rev. Mod. Phys. 71 (1999) 897.
[12] S. Le Bohec, et al., Nucl. Instr. and Meth. A 416 (1998) 425.
[13] M.F. Cawley, et al., Exp. Astron. 1 (1990) 173. EGRET web site: egret.sao.arizona.edu/index.html
[14] A. Barrau, et al., Nucl. Instr. and Meth. A 416 (1998) 278–292. CAT web site: www-lpnhep.in2p3.fr/homecat/
[15] T. Hara, et al., Nucl. Instr. and Meth. A 332 (1993) 300–309. CANGAROO web site: http://icrhp9.icrr.u-tokyo.ac.jp/index.html
[16] A. Daum, et al., Astropart. Phys. 8(1–2) (1997) 1. HEGRA web site: www.mpi-hd.mpg.de/hfm/CT/CT.html
[17] GLAST web site: http://glast.stanford.edu/
[18] A. Morselli, et al., Nucl. Phys. B 85 (2000) 22–27. AGILE web site: http://www.roma2.infn.it/infn/agile/
[19] B. Alpat, Nucl. Instr. and Meth. A 461 (2001) 272.
[20] R. Enomoto, et al., Astropart. Phys. (2001), to appear. CANGAROO3 web site: http://icrhp9.icrr.u-tokyo.ac.jp/c-iii.html
[21] W. Hofmann, in: B.L. Dingus, M.H. Salomon, D.B. Kieda (Eds.), Towards a Major Atmospheric Cherenkov Detector—VI, Snowbird, 1999, p. 500. HESS web site: http://www.mpi-hd.mpg.de/hfm/HESS/HESS.html
[22] VERITAS web site: http://veritas.sao.arizona.edu/
[23] J.A. Barrio, the MAGIC telescope, Max-Planck-Institute Report MPI-PHE/98-5. MAGIC web site: http://hegra1.mppmu.mpg.de/MAGICWeb
[24] C.L. Bhat, et al., in: Towards a Major Atmospheric Cherenkov Detector—V, Krugar National Park, South Africa, 1997, pp. 323–327.
[25] S.M. Oser, et al., Astrophys. J. 547 (2000) 949; S.M. Oser, et al., Ph.D. Thesis, University of Chicago, August 2000. http://hep.uchicago.edu/oser/

[26] F. Arqueros, et al., Astropart. Phys., to be published. Preprint: astro-ph/0108270.
[27] J.A. Zweerink, et al., Proceedings of the 26th ICRC 5, 1999, p. 223. SOLAR2 web site: solartwo.ucr.edu/solar2.html
[28] B. Giebels, et al., Nucl. Instr. and Meth. A 412 (1998) 329.
[29] S. Danaher, et al., Sol. Energy 28 (1982) 335.
[30] T.O. Tümer, et al., Nucl. Phys. B 14A (1990) 351.
[31] M. de Naurois, Ph.D. Thesis, Université Paris VI, May 10, 2000. http://polywww.in2p3.fr/celeste/these/These.html
[32] N. Hérault, Ph.D. Thesis, Université Louis Pasteur, Strasbourg, April 14, 2000. http://www.lal.in2p3.fr/presentation/bibliotheque/publications/Theses00.html
[33] M. de Naurois, et al., Astrophys. J. 566 (2002).
[34] M.F. Cawley, in: R.C. Lamb (Ed.), Towards a Major Atmospheric Cherenkov Detector II, Calgary, Canada, July 17–18, 1993, p. 176.
[35] M.P. Kertzman, G.H. Sembrosky, Nucl. Instr. and Meth. A 343 (1994) 329.
[36] R. Winston, J. Opt. Soc. Amer. 60 (1970) 245.
[37] M. de Naurois, et al., Proceedings of the 26th ICRC, 1999, OG.4.3.06.
[38] ETEP web site: www.etep.com
[39] J. Holder, et al., in: F.A. Aharonian, H. Voelk (Eds.), Heidelberg Gamma Ray Symposium, 2000, p. 635.
[40] R. Le Gallou, Ph.D. Thesis, Université Paris XI, September 24, 2000. Available at: http://infodan.in2p3.fr/themis/CELESTE/PUB/papers.html